RESEARCH ARTICLE
SPACE PHYSICS: IONOSPHERIC PHYSICS

Earth and Planetary Physics
11: 1–9, 2027
doi: 10.26464/epp2027004

Sporadic E conditions associated with four spread F morphologies over Hainan: Local-time-adjusted and seasonal comparisons

Zheng Wang[1,2], JiaXuan Zhang[3], GuoJun Wang[1,2*], JianKui Shi[1,2,4], JinHui Cai[3], ZhengWei Cheng[1,2], Quan Qi[3,5], PengDong Gao[5], and Xiao Wang[1,2]

[1]State Key Laboratory of Solar Activity and Space Weather, National Space Science Center, Chinese Academy of Sciences, Beijing 100190, China;

[2]Hainan National Field Science Observation and Research Observatory for Space Weather, National Space Science Center, Chinese Academy of Sciences, Beijing 100190, China;

[3]State Key Laboratory of Media Convergence and Communication, Communication University of China, Beijing 100024, China;

[4]University of Chinese Academy of Sciences, Beijing 100049, China;

[5]Key Laboratory of Media Audio & Video (Communication University of China), Ministry of Education, Beijing 100024, China

Key Points:

- Range and strong range spread F accompany weaker sporadic E after adjustment for the usual temporal background.
- Frequency and mixed spread F show seasonal changes in the probability of measuring sporadic E.
- For frequency and mixed spread F, the sporadic E virtual heights are higher than the nonevent background in summer and lower in autumn.

Citation: Wang, Z., Zhang, J. X., Wang, G. J., Shi, J. K., Cai, J. H., Cheng, Z. W., Qi, Q., Gao, P. D., and Wang, X. (2027). Sporadic E conditions associated with four spread F morphologies over Hainan: Local-time-adjusted and seasonal comparisons. *Earth Planet. Phys.*, *11*(1), 1–9. http://doi.org/10.26464/epp2027004

Abstract: Sporadic E (Es) can modify the electrodynamic conditions for F-region irregularities, yet observations have reported both positive and negative relationships with spread F (SF). Distinguishing SF morphologies may help explain this variation. We analyze 230,157 quarter-hour ionosonde records from Hainan from 2014 to 2020, comparing range, strong range, frequency, and mixed SF with non-SF observations. Spread F labels were inferred using one classification algorithm throughout the record, whereas the E-region parameters were exported after manual revision of the ionogram traces. Harmonic models account for local-time, seasonal, and annual variations. We examine both the probability of measuring E/Es parameters and their values relative to the non-SF background, with uncertainty estimated by resampling local dates and groups of consecutive days. Range and strong range SF accompany less frequently measured Es and lower *f*oEs (Es critical frequency). Their adjusted *f*oEs differences are approximately −0.27 and −0.26 MHz, and both associations with weaker Es occur in all four seasons. Frequency and mixed SF accompany more frequently measured Es in winter, spring, and autumn. In summer, the frequency SF association becomes negative, whereas mixed SF is close to the non-SF reference. These two forms also accompany higher Es virtual heights in summer and lower values in autumn. Ordinary E critical-frequency differences are small and more sensitive to the treatment of measurement availability. The observations suggest that Es density and its vertical or propagation environment contribute different information about the conditions accompanying SF. We discuss weaker Es as a possible favorable background for some range-spreading irregularities and seasonally changing Es structure and polarization fields as possible contributors to the other associations.

Keywords: spread F; sporadic E; ionosonde; low-latitude ionosphere; seasonal variation; E–F region coupling

1. Introduction

Sporadic E (Es) consists of thin layers of enhanced ionization in the E region. At low and middle latitudes, neutral-wind shear can concentrate long-lived metallic ions into these layers, producing marked daily and seasonal variations (Haldoupis, 2011). Observations have linked Es to spread F (SF), but the relationship varies among observational conditions. Lee CC and Chen WS (2018) found that stronger *f*oEs (Es critical frequency) and a larger difference between *f*oEs and *f*bEs (Es blanketing frequency) were associated with more frequent nighttime SF at a midlatitude station. The Conjugate Point Equatorial Experiment (COPEX) in South America, however, found no simple correspondence between equatorial SF and Es at conjugate E-region locations (Reinisch et al., 2004).

These observations can be considered in terms of more than one

First author: Z. Wang, zwang@swl.ac.cn
Correspondence to: G. J. Wang, gjwang@nssc.ac.cn
Received 17 SEP 2026; Accepted 25 OCT 2026.
First Published online 24 NOV 2026.
©2026 by Earth and Planetary Physics.

electrodynamic process. Increased E-region conductance can weaken the conditions favorable for equatorial SF, including through changes to the evening electric field (Stephan et al., 2002). In contrast, coordinated observations at midlatitudes have associated patchy Es with disturbances in the F region (Kelley et al., 2003). A wind-driven polarization field generated within an Es patch can provide a physical connection between the two regions (Shalimov and Haldoupis, 2005). The structure of Es, magnetic geometry, and surrounding ionospheric state may therefore affect its relationship with SF. These factors motivate comparing the E-region conditions accompanying different visible F-region forms.

Hainan lies at approximately 11°N magnetic latitude, within the low-latitude ionosphere influenced by equatorial electrodynamics. Bubble-related irregularities have been observed there together with strong range SF (SSF) (Wang GJ et al., 2015), whereas its local Es layer also samples the wind-driven E-region environment. This setting allows us to examine how Es conditions accompany different SF forms away from the magnetic equator. Earlier observations at the station distinguished range SF (RSF), SSF, frequency SF (FSF), and mixed SF (MSF) and showed that their preferred local times and seasons differ (Wang GJ et al., 2010). Nearby observations at Sanya also showed that SF can occur without concurrent global positioning system (GPS) scintillation, with Es and medium-scale traveling ionospheric disturbances proposed as contributors during the June solstice (Zhang Y et al., 2015). A comparison among SF forms therefore has physical relevance in this low-latitude region. Their different occurrence times also mean that an unadjusted comparison of E/Es parameters could reproduce the usual daily or seasonal cycle instead of a condition specifically associated with SF.

Here we examine the E/Es conditions accompanying four SF forms in a unified Hainan record for 2014–2020. We ask whether the probability of measuring E/Es parameters and their measured values differ from non-SF observations after accounting for local time, season, and year. Separating these two questions distinguishes changes in the availability of an ionospheric trace from changes in the parameters measured from it. We then examine whether the associations vary by season. The aim is to describe the E-region environments accompanying different SF forms and use those patterns to assess possible links with F-region irregularities.

2. Data and Methods

2.1 Observations and SF Classification

The observations come from the Chinese Meridian Project station at Hainan Fuke (geographic coordinates 19.5°N, 109.1°E; magnetic latitude 11°N), which lies at low geographic and geomagnetic latitudes. Its location allows observations of irregularities associated with the equatorial ionization anomaly region while also sampling E-region structures influenced by the lower thermosphere. This combination makes Hainan useful for examining how the E-region environment differs among visible forms of F-region irregularity.

We analyzed the Hainan ionosonde observations from 2014 to 2020 as one continuous series. Spread F morphology was identified using the classification method of Wang Z et al. (2023), with the related ionogram dataset described by Gao PD et al. (2026). The categories were RSF, SSF, FSF, MSF, and non-SF.

Two of the authors (GuoJun Wang and Zheng Wang) manually reviewed the ionograms and revised the traces used to derive the E/Es parameters. The revised traces were processed with the Automatic Real-Time Ionogram Scaler (ARTIST) 5002 in SAO Explorer 3.4.17. We analyzed the E- and Es-layer critical frequencies, *f*oE and *f*oEs (MHz), and the Es virtual height, *h*′Es (km).

To prevent intervals with denser observations from receiving greater weight, the main analysis used the 230,157 records falling exactly on the Coordinated Universal Time (UTC) quarter-hour grid. Local time (LT) denotes local mean solar time, calculated from the recorded UTC, used here as universal time (UT): LT = UT + (109.1°/15°) h = UT + 7 h 16 min 24 s, with the date advanced when the sum crosses midnight. Source years were retained for adjustment of annual differences, and local calendar dates were used to group observations for resampling. All 7 years contributed to one main analysis.

The morphology labels describe how the F-region echo is spread on a frequency–height ionogram. Range SF is dominated by range broadening, particularly at lower sounding frequencies, whereas FSF broadens near the F_2 critical frequency. Mixed SF contains both characteristics. Strong range SF denotes particularly extensive range spreading and is treated as a separate low-latitude class in the Hainan classification (Shi JK et al., 2011; Wang Z et al., 2023).

The current Chinese Meridian Project catalog lists the station as Danzhou; its parameter-product record is Ionospheric Parameters of Ionospheric Digital IonoSonde at Danzhou Station (https://doi.org/10.12176/01.06.00508-V01). This current catalog record is distinct from the historical 2014–2020 series analyzed here. Table 1 summarizes the comparison groups and the measurements available for each parameter.

Table 1. Observations and available E/Es measurements on the primary quarter-hour grid. Counts are records, not independent events.

SF form	Records	Measured *f*oE	Measured *f*oEs and *h*′Es
non-SF	176316	83287	108389
RSF	20523	3707	7287
SSF	9738	1315	3050
FSF	15653	1661	8073
MSF	7927	692	4429

2.2 Probability of Measuring E and Es Parameters

E and Es parameters vary strongly with local time and season. We therefore compared SF and non-SF observations after accounting for these temporal variations. Separate logistic models described whether *f*oE could be measured and whether the Es parameter pair, *f*oEs and *h*′Es, could be measured. Each model included indicators for the four SF types, with non-SF as the reference, source-year terms, eight daily harmonics, four annual harmonics, and first-

order daily-annual modulation. The harmonics described the recurring temporal background with a continuous periodic curve. The fixed orders allowed several-hour variation within the day and broad structure within the seasonal cycle; their basis and first-order modulation are explained in Section S2. The SF coefficients were expressed as odds ratios. We also calculated the average difference in predicted measurement probability between each SF type and non-SF over the temporal conditions represented in the fitted sample, reported in percentage points.

2.3 Measured Parameter Values Relative to the Non-SF Background

The four SF forms occur preferentially at different local times and seasons, whereas E/Es parameters also vary over the day and year. A comparison of their raw values could therefore reflect the normal ionospheric cycle. We used non-SF observations to estimate the usual parameter level for each observation time and year, then subtracted this background to ask whether the E/Es conditions accompanying each SF form departed from that expected level. We compared parameter values only where the corresponding quantity was measured. For *f*oE, *f*oEs, and *h*′Es separately, a robust harmonic model fitted to non-SF observations described the usual local-time, seasonal, and annual background. The model used the same temporal terms as the probability analysis. Huber regression (Huber, 1964) reduced the influence of unusually large residuals, and a ridge penalty of 1.0 was applied to the harmonic coefficients. The Huber threshold was 1.5 times the residual scale. After subtracting this background from the measured values, we calculated the median residual for each SF type and subtracted the median residual of the non-SF observations. These differences describe whether the measured parameters accompanying SF were higher or lower than their usual temporal background.

Figure S1 displays the measured non-SF background and the fitted values at the same observation times. Within each season, measurements are summarized in one-hour local-time bins, pooling the full 2014–2020 record. The observed median and interquartile range are shown alongside the median fitted value so that the daily and seasonal variations removed before the SF comparison could be seen directly. We also counted non-SF reference dates within each year, season, and one-hour local-time interval occupied by an SF measurement. These counts showed where the background comparison had direct observational coverage (Table S8).

2.4 Uncertainty and Sensitivity Analyses

Successive ionograms may share the same ionospheric conditions. We therefore resampled complete local dates, rather than individual ionograms, to describe sampling uncertainty. Dates were drawn with replacement separately within each local calendar year, and all records from a selected date retained the same multiplicity. The logistic probability models were refitted for each resample. For parameter values, we recalculated the SF and non-SF residual medians while retaining the fitted non-SF background. The resulting parameter intervals describe uncertainty in the residual comparison conditional on that background. Each main comparison used 2000 resamples.

To examine whether continuity across midnight or over successive nights affected the annual comparisons, we repeated the resampling using days beginning at local noon and nonoverlapping 3-day groups beginning at noon. Each grouping contained 2000 resamples. A separate 2000-resample calendar-date calculation provided a comparison with the original grouping. Within each resample, the parameter differences were calculated both with the original non-SF background and with that background refitted to the resampled non-SF observations. This paired comparison included uncertainty in the estimated background. The seasonal extension of this paired comparison is described in Section 2.5. Full definitions and results are given in Section S4.1 and Tables S5–S6.

The two sets of main comparisons address different questions: eight comparisons concern measurement probability, and 12 concern measured parameter values. We applied the Benjamini–Hochberg adjustment (Benjamini and Hochberg, 1995) separately to these sets. Effect sizes and their 95% intervals are reported together, with detailed resampling and probability calculations in the supplementary methods. Year-by-year omission examined whether the overall patterns were dominated by a single year. An additional analysis excluded the years involved in classifier development and evaluation, retaining 2017–2020. These comparisons used the same observing series and did not define separate instrumental or labeling periods.

We also examined the influence of sampling density and time conventions by using all native observations, shifting the quarter-hour sampling phase by 5 min where observations existed, shifting local time by half an hour, and excluding records for which the source year differed from the local calendar year. To assess whether unequal chances of measuring a parameter influenced its residual distribution, we repeated the median comparison with inverse measurement-probability weights, limited to the first and 99th percentiles. These analyses compared effect directions and magnitudes; their full estimates and sample counts are retained in the supplementary tables.

2.5 Seasonal Associations

Seasonal comparisons examined whether a given SF form accompanied different E/Es conditions at different times of year. Winter, spring, summer, and autumn comprise December–February, March–May, June–August, and September–November, respectively, according to local dates. The probability models retained the temporal terms of the main analysis and added seasonal terms and SF-type-by-season indicators. Standard errors were clustered by local date, and Wald tests compared the coefficients across seasons for each SF type. For measured parameters, the primary non-SF background was subtracted first; residual median differences were then calculated separately within each season. Their intervals used 2000 date-cluster resamples. These seasonal analyses were exploratory, with separate multiple-comparison adjustments for probability contrasts, parameter contrasts, and seasonal coefficient tests. To assess whether the seasonal Es patterns depended on the estimated background, we additionally

completed 2000 noon-based 3-day resamples for *f*oEs and *h*′Es, calculating each seasonal difference with both a fixed and a refitted background. In the same draws, we subtracted the autumn difference from the summer difference for each parameter and SF form. The 32 seasonal comparisons and eight direct summer–autumn comparisons received separate Benjamini–Hochberg adjustments within each background treatment (Section S7.1 and Table S7).

3. Results

3.1 E and Es Conditions Relative to the Non-SF Background

Figure 1 shows that the probability of measuring Es has opposite associations with the two range-spreading forms and with FSF and MSF. After time and year adjustment, Es is less likely to be measured during RSF and SSF but more likely during FSF and MSF. The probability differences relative to non-SF are approximately −6.4 and −10.3 percentage points for RSF and SSF, compared with +4.1 and +7.2 percentage points for FSF and MSF. Their 95% intervals lie on the corresponding sides of zero (Table S1). Thus, the annual record does not show a single Es association shared by all four forms: reduced Es measurement probability accompanies the range-spreading forms, whereas increased probability accompanies FSF and MSF.

The measured *f*oEs values provide a complementary view. Figure 1d places RSF and SSF to the left of the non-SF reference, with median differences of −0.27 MHz (95% interval −0.31 to −0.24 MHz) and −0.26 MHz (−0.30 to −0.20 MHz). Thus, these forms accompany both less frequently measured Es and a weaker measured layer. Frequency SF illustrates why measurement probability and strength should be examined separately: Es is measured more often overall, whereas the small annual *f*oEs difference is close to the temporal background; its uncertainty is examined further in Section 3.3. Mixed SF instead accompanies a positive *f*oEs difference of 0.12 MHz (0.05 to 0.21 MHz). The combined probability and frequency results identify a weaker Es environment during RSF and SSF, whereas the increased measurement probability during FSF need not involve an increase in layer intensity.

Figure 1e shows higher *h*′Es during RSF, FSF, and MSF, with median differences of roughly 1–2.4 km. Strong range SF lies close to the reference, and its interval spans zero. Ordinary E differs less consistently from the background. In Figure 1a, *f*oE is more often measured during RSF and SSF, less often during MSF, and close to the non-SF probability during FSF. Where *f*oE is measured, all four primary residual differences are small and negative, approximately −0.03 to −0.06 MHz (Figure 1c). Their sensitivity to measurement availability is considered in Section 3.3. Overall, Es provides the more coherent association with SF morphology; its measurement

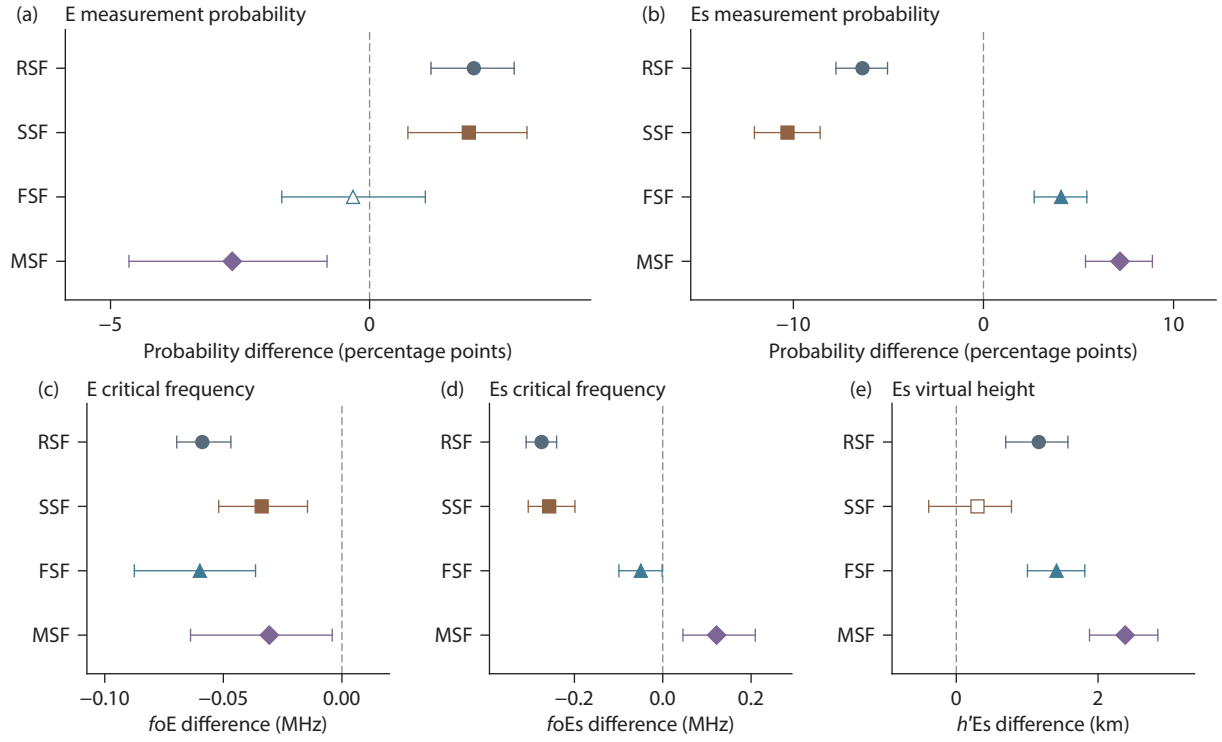

Figure 1. Differences in E/Es conditions between each SF form and non-SF observations over Hainan, 2014–2020. Panels (a) and (b) show adjusted probability differences for measuring *f*oE and the *f*oEs/*h*′Es pair. Panels (c), (d), and (e) show differences in median residuals after subtraction of the fitted non-SF temporal background. The horizontal bars are 95% percentile intervals from 2000 resamples of local dates within years; parameter intervals are conditional on the fitted background. The symbols *p* and *q* denote unadjusted and Benjamini–Hochberg-adjusted *p*-values, respectively. Filled symbols indicate $q < 0.05$ within the eight probability or 12 parameter comparisons; open symbols show the remaining estimates. The zero lines mark the non-SF reference. Table 1 gives measurement counts and Table S1 gives effect sizes, intervals, and numbers of dates. *h*′Es denotes virtual height.

probability, critical frequency, and virtual height describe complementary aspects of the E-region environment.

3.2 Seasonal Variation of the Es Associations

Figure 2 shows which features persist across seasons and which are obscured by the annual average. Range SF and SSF remain below the non-SF reference in both Es measurement odds and *f*oEs in winter, spring, summer, and autumn. Their association with weaker Es therefore extends across the seasonal cycle. Frequency SF and MSF have higher measurement odds in winter, spring, and autumn, whereas the summer estimates approach or fall below the reference. The summer odds ratio is approximately 0.81 for FSF and 1.00 for MSF. Seasonal coefficient comparisons identify variation in the measurement association for SSF, FSF, and MSF; the RSF variation is less clearly distinguished (Table S3).

The frequency differences in Figure 2b help distinguish more frequently measured Es from stronger Es. Frequency SF has lower *f*oEs in summer, whereas the winter and spring differences are close to zero. Mixed SF accompanies higher *f*oEs in winter and spring but little departure from the reference in summer. The positive autumn frequency estimates for FSF and MSF are less clearly separated from zero after the seasonal multiple-comparison adjustment (Table S2). The recurring feature is a seasonal change in the combination of measurement probability and layer intensity, rather than a uniform increase for all SF forms.

The virtual-height panel adds another seasonal feature. Frequency SF and MSF accompany higher *h*′Es in summer but lower *h*′Es in autumn. The summer differences are approximately +3.1 and +3.6 km, respectively, compared with −1.7 and −1.3 km in autumn. This contrast remains clear when the non-SF background is refitted and observations are resampled in 3-day groups. The direct comparison places their summer height deviations approximately 5 km above their autumn deviations (Table S7). Range SF has its clearest positive height differences in winter and spring; SSF stays close to the background in each season. These population differences describe a seasonal change in the

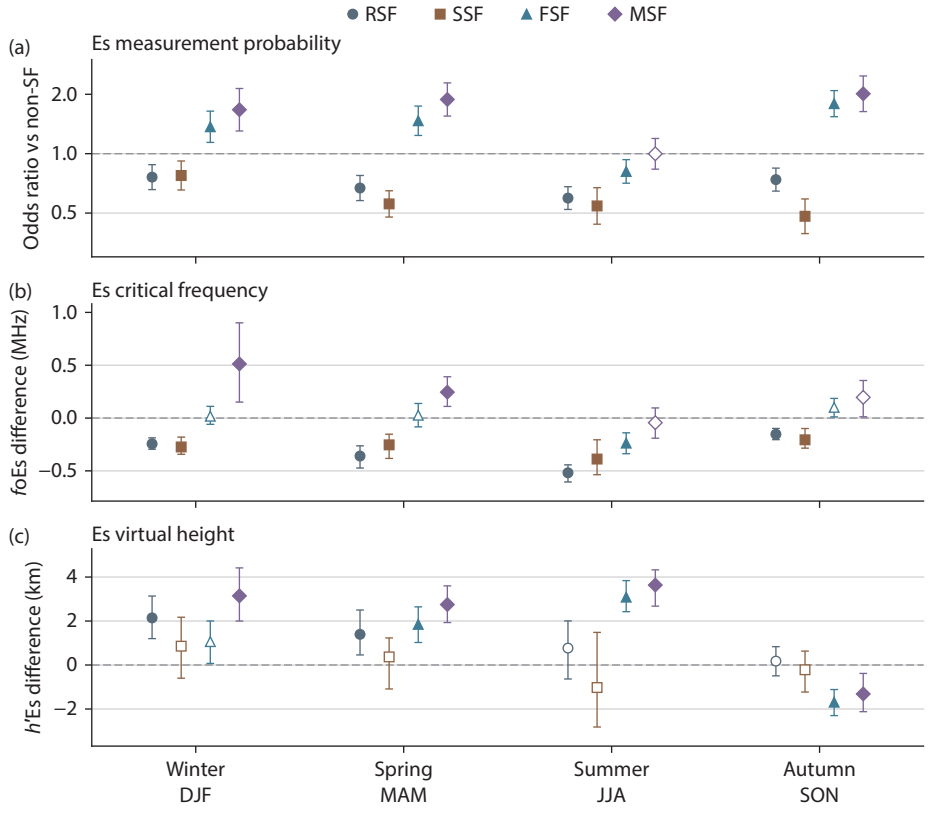

Figure 2. Seasonal Es conditions accompanying four SF forms, relative to non-SF observations in 2014–2020. (a) Odds ratios for measuring the pair *f*oEs and *h*′Es, after accounting for local time, season, and source year. The vertical scale is logarithmic. (b, c) Differences in median *f*oEs and *h*′Es residuals after subtracting the non-SF temporal background. Error bars in (a) are 95% Wald intervals with standard errors clustered by local date. Those in (b) and (c) are 95% percentile intervals from 2000 resamples of local dates within years, conditional on the fitted non-SF background. The symbols p and q denote unadjusted and Benjamini–Hochberg-adjusted p-values, respectively. Filled symbols denote $q < 0.05$ after Benjamini–Hochberg adjustment over all 32 seasonal measurement-probability comparisons or all 48 seasonal parameter comparisons, respectively. The adjustment includes all planned combinations, with $p = 1$ assigned to those with insufficient observations (Section S7). Open symbols show the remaining estimates, not missing data. The horizontal reference lines indicate no difference from non-SF. DJF, MAM, JJA, and SON denote December–February, March–May, June–August, and September–November. Sample sizes and numbers of local dates are provided with the source data; *h*′Es is virtual height. Paired 3-day resampling with background refitting and direct summer–autumn comparisons are given in Table S7.

typical virtual reflection height accompanying SF. Together, the panels describe weaker Es throughout the year during RSF and SSF and a seasonally changing combination of Es intensity and reflection conditions during FSF and MSF.

3.3 Influence of Data Coverage and Measurement Availability

The broad Es-frequency pattern changes little when individual years are omitted or measurement-probability weights are applied: RSF and SSF retain lower *f*oEs, and MSF retains higher *f*oEs wherever the comparison has sufficient observations. The ordinary E layer shows a less distinct pattern. During FSF and MSF, *f*oE remains close to its usual level: it is slightly lower in the main comparison and slightly higher after allowing for unequal measurement opportunities. Sporadic E virtual height during SSF also stays close to the non-SF background across the comparisons. The modestly higher Es virtual height accompanying RSF in the full record is not repeated in the 2017–2020 subset, where it is slightly lower. We therefore focus the physical discussion on the Es-frequency and seasonal patterns, rather than proposing a common ordinary-E reduction or a universal height increase.

The additional time-group and background calculations preserve the main Es pattern (Table S5). Range SF and SSF accompany less frequently measured Es and lower *f*oEs, whereas MSF accompanies higher *f*oEs. With 3-day groups and a refitted background, the *f*oEs intervals are −0.32 to −0.22 MHz for RSF, −0.31 to −0.20 MHz for SSF, and 0.02 to 0.22 MHz for MSF. The small annual *f*oEs difference for FSF is less clearly distinguished: its interval includes zero under all three groupings when the background is refitted. Higher *h*′Es during RSF, FSF, and MSF also remains clear in these annual comparisons, whereas the SSF height difference stays close to zero. Thus, the contrast between more frequent Es measurements and greater Es intensity remains important, especially for FSF.

The non-SF observations cover the years, seasons, and local-time intervals in which Es was measured during all four SF forms (Table S8). The 5-min-offset sample represents a different mix of observing conditions: its FSF observations contain proportionally more autumn and fewer spring records than the primary sample, and all come from 2017 to 2020 (Table S9). Only the FSF Es-measurement comparison has sufficient coverage in this sample, where the association is slightly negative instead of positive. The offset comparison thus describes a smaller population with different seasonal and annual coverage, alongside the shift in observing time. The 2017–2020 auxiliary analysis also leaves some comparisons sparsely measured; the main analysis continues to use all 7 years.

4. Discussion

4.1 E-region Conditions Accompanying RSF and SSF

The clearest result for RSF and SSF is the combination of less frequently measured Es and lower *f*oEs in all four seasons. Because the comparison removes the usual time-dependent background, this association is not simply the consequence of RSF and SSF occurring preferentially when Es is seasonally weak. It indicates that these forms tend to accompany weaker Es even relative to the conditions normally observed at those times. This direction is consistent with the electrodynamic calculations of Stephan et al. (2002): stronger Es can inhibit equatorial irregularity growth, especially when it reduces the evening upward plasma drift. Their model found that a large direct conductivity effect required unusually dense Es. The Hainan result therefore points most naturally to weaker Es as part of an environment favorable for F-region growth through the coupled electric field, rather than requiring strong direct suppression by the measured local layer. These weak-Es conditions provide specific targets for joint measurements of the local layer, F-region drift, and conductance in the magnetically connected E regions.

Abdu et al. (2003) provided a complementary interpretation of the same negative association. At Fortaleza, Brazil, stronger evening prereversal enhancement accompanied Es disruption, suggesting that an electric-field change can simultaneously favor F-region irregularities and weaken Es. Our lower *f*oEs during RSF and SSF is compatible with this shared response as well as with reduced E-region loading. The two explanations connect the observed weak-Es state to the growth environment from different directions: Es may modify the field, or the coupled field may modify both layers. The Hainan cases of Wang GJ et al. (2015), in which SSF accompanied satellite plasma depletions and GPS scintillation, make bubble-related electrodynamics particularly relevant for SSF. The present 7-year comparison adds a recurring E-region association to those case observations. Establishing whether Es weakens before or during enhanced F-region drift would distinguish its role in preparing the growth conditions from its response to the same electrodynamic change.

4.2 Seasonal Changes in FSF and MSF

For FSF and MSF, the positive annual Es-measurement association combines different seasonal conditions. Mixed SF accompanies higher *f*oEs in winter and spring, consistent in direction with the positive relation between Es intensity and nighttime SF reported by Lee CC and Chen WS (2018) at a midlatitude station. Frequency SF, however, has near-background *f*oEs in winter and spring despite more frequent Es measurements. In summer, its Es-measurement association becomes negative, whereas MSF approaches the non-SF reference. More frequent Es measurements and a stronger measured layer are therefore distinct features, and their combination depends on SF form and season. Latitude offers a possible physical explanation for the difference from the midlatitude study. At Hainan, bubble-related irregularities influenced by equatorial electric fields contribute to the SF population (Wang GJ et al., 2015); midlatitude Es–SF coupling can instead involve polarization fields generated in wind-driven Es patches (Shalimov and Haldoupis, 2005). These processes can give different associations between local Es intensity and SF. The comparison also differs statistically: Lee CC and Chen WS (2018) examined nighttime SF occurrence in relation to Es characteristics, whereas we compare E/Es conditions among four SF forms after temporal adjustment. The observed differences may therefore reflect both the contributing irregularity populations and the conditions being compared.

The summer result gives a specific context for the nearby Sanya

observations of Zhang Y et al. (2015), who proposed Es and medium-scale traveling ionospheric disturbances as contributors to SF without GPS scintillation. Our FSF and MSF results suggest that such an Es contribution should be sought in its structure and electrodynamic setting, rather than in a general increase of *f*oEs. This interpretation also links the summer-to-autumn reversal of their virtual-height differences to the coupled disturbances observed by Kelley et al. (2003) and the wind-driven Es-patch polarization model of Shalimov and Haldoupis (2005). A patch-generated field depends on layer structure and neutral winds as well as density; a higher peak density alone is consequently not a sufficient description of its coupling to the F region. Tsunoda (2007) similarly proposed that an Es-generated perturbation can seed a plasma bubble when the F-region background allows it to grow. Together, these studies make the seasonal combination of *f*oEs and *h*′Es physically informative: it may identify changing conditions for producing and transmitting perturbations, even when the average Es intensity is close to the non-SF background. Spatial Es observations, winds, and F-region drift would allow this interpretation to be tested directly.

4.3 Es Virtual Height and the Seasonal Environment

Figure 2 also shows higher *h*′Es during FSF and MSF in summer, followed by lower values relative to non-SF observations in autumn. The direct summer–autumn comparison shows that this change persists after removing each season's usual background. It therefore characterizes the Es environment accompanying these SF forms and draws attention to reflection height and propagation conditions, alongside critical frequency. Haldoupis (2011) reviewed how tidal wind shear controls the formation and descent of metallic-ion layers. A seasonally changing wind field could therefore contribute to the different Es environments accompanying SF. The present comparison concerns virtual height, which contains group-delay effects as well as information about the reflecting layer. Joint measurements of neutral winds and resolved layer profiles would help determine whether the seasonal differences arise mainly from layer position, density structure, or radio-wave propagation below Es.

The interpretation of *f*oEs also benefits from separating the ordinary E background from the enhanced layer. Haldoupis (2019) showed that *f*oEs includes contributions from both ordinary E-region plasma and the metallic-ion layer and proposed a correction based on the International Reference Ionosphere (IRI). Our subtraction of the non-SF time-dependent background addresses a different question: whether an SF form accompanies an unusual measured parameter for that time and season. It retains the observed quantity without converting it into a metallic-ion density. Together, the frequency and virtual-height comparisons describe an E-region environment that can guide coordinated observations of Es structure, F-region drifts, and irregularities.

4.4 Interpretation of the Measured E-region Conditions

The ordinary-E comparison helps place the Es associations in context. The *f*oE remains close to its usual level, and its small differences change with measurement availability. In contrast, the range-spreading forms consistently accompany lower *f*oEs, whereas FSF and MSF show distinct seasonal combinations of Es intensity and virtual height. This finding favors examining the enhanced layer and its structure when interpreting E–F relations. Differences in SF populations and seasonal coverage may consequently contribute to the different signs reported in earlier Es–SF studies.

4.5 Further Observations

A single ionosonde samples the E/Es conditions near Hainan, whereas the electrodynamic environment of F-region irregularities also involves spatial structure and magnetically connected regions. Our observations do not resolve horizontal Es gradients, conjugate E-region conductance, or the electric fields and winds linking the layers. The associations therefore describe the local environments accompanying SF; their latitude dependence and the direction of E–F coupling remain questions for coordinated observations.

The seasonal associations suggest a focused strategy for coordinated measurements. Nights with RSF or SSF and a weak Es state are useful for examining the relation between E-region electrical loading and F-region drift. Nights with FSF or MSF are particularly useful for comparing summer with autumn, when their *h*′Es differences have opposite signs. Airglow images and spatially distributed ionosonde measurements could reveal whether these conditions accompany Es patches and traveling structures. The multistation observations of Reinisch et al. (2004) showed that a simple Es–SF correspondence does not hold across conjugate locations, highlighting the importance of observing the connected regions rather than relying on a single local layer measurement.

The F-region conditions should be measured alongside Es. Rocket and radar observations identified strong velocity shear and structured bottomside plasma near SF onset (Hysell et al., 2005). Abdu et al. (2018) showed that disturbance electric fields can enhance or oppose the evening vertical drift and thereby change SF development. These results motivate comparing Es structure with drift, winds, and the preceding geomagnetic conditions. The current time-background models account for recurring daily and seasonal variations and differences among years. Explicit measurements of the electric field and event-scale external forcing would make it possible to examine how similar Es conditions lead to different F-region outcomes.

5. Conclusions

The Hainan observations show that four SF morphologies accompany different E/Es conditions after adjustment for local time, season, and year. Range SF and SSF are associated with less frequently measured Es and lower *f*oEs across all four seasons. A weaker Es state may accompany conditions favorable for F-region irregularities through reduced electrical loading or a common electrodynamic response in the two regions.

Frequency SF and MSF have more seasonally variable associations. Compared with non-SF observations, Es was more likely to be measured during FSF and MSF in winter, spring, and autumn. In summer, this probability was lower during FSF and close to the

non-SF level during MSF. Their *h*′Es differences also change from positive in summer to negative in autumn. These features draw attention to the structure and propagation environment of Es, as well as its density, when interpreting possible E–F connections.

Sporadic E intensity, measurement probability, and virtual height distinguish the E-region conditions accompanying different SF forms and seasons. Coordinated measurements of Es structure, neutral winds, F-region drift, and conjugate regions can build on these seasonal and morphological distinctions to examine how initial perturbations and growth conditions act together.

Author contributions

Zheng Wang: Conceptualization, Methodology, Data curation (manual ionogram review and trace revision), Formal analysis, Writing—original draft. JiaXuan Zhang: Data curation, Formal analysis, Visualization. GuoJun Wang: Conceptualization, Methodology, Data curation (manual ionogram review and trace revision), Formal analysis, Writing—review and editing. JianKui Shi: Methodology, Writing—review and editing. JinHui Cai: Data curation, Formal analysis, Visualization. ZhengWei Cheng: Validation, Writing—review and editing. Quan Qi: Data curation. PengDong Gao: Validation, Writing—review and editing. Xiao Wang: Investigation, Resources, Data curation, including instrument operation and data processing.

Acknowledgments

This research was supported by the National Key R&D Program of China (Grant No. 2025YFF0510703, awarded to GJ Wang); the Youth Innovation Promotion Association of the Chinese Academy of Sciences (Grant No. 2023000116, awarded to Z Wang); the Deployment Project of the Overseas Science and Education Cooperation Center, Bureau of International Cooperation, Chinese Academy of Sciences (Grant No. 119GJHZ2024027MI, awarded to ZW Cheng); the Specialized Research Fund for State Key Laboratories (awarded to Z Wang); the Pandeng Program of the National Space Science Center, Chinese Academy of Sciences; and the Chinese Meridian Project. We acknowledge the Chinese Meridian Project for the historical Hainan Fuke ionosonde observations used in this study. The project data-access service is https://dcstatus.meridianproject.ac.cn/; its current Danzhou parameter-product catalog is identified by https://www.doi.org/10.12176/01.06.00508-V01, as distinguished from the historical study series in Open Research. We thank the staff of the Chinese Meridian Project (https://cstr.cn/31122.02.MSP) for their technical support and assistance in data collection and analysis.

Open Research

The observations were collected at Hainan Fuke within the Chinese Meridian Project. The project data-access service is https://dcstatus.meridianproject.ac.cn/. The station is listed as Danzhou in the current parameter-product catalog (https://doi.org/10.12176/01.06.00508-V01). That catalog record currently covers 2023–2026; enquiries about the historical 2014–2020 observations should be directed to the project data-access service. This study uses E/Es parameter series obtained following manual ionogram review and trace revision by GJ Wang and Z Wang. These manually processed series are not redistributed in ScienceDB.

Aggregate results, figure source data, analysis code, and documentation are archived in ScienceDB, Version 1, by Wang Z and Wang GJ (2026; https://doi.org/10.57760/sciencedb.012m9). The dataset is published with restricted file access. Figure S1 and Tables S1–S9 are also available in the Supplementary Materials. Requests can be submitted through the ScienceDB Data Access Application by providing the applicant's name, institutional affiliation, and intended research use, for review by the dataset corresponding author, Z Wang (zwang@swl.ac.cn). The archive contains statistical summaries rather than individual observations. The SF classification method is described by Wang Z et al. (2023) and related ionogram resources by Gao PD et al. (2026). Original ionograms, manually revised traces, individual E/Es/F-region parameter records, per-observation SF labels, and classifier weights are not redistributed in this archive.

Computational Assistance

OpenAI Codex assisted with code development and checking, manuscript organization, and language editing. The authors are responsible for checking the analyses, references, and scientific interpretation in the final manuscript.

References

Abdu, M. A., MacDougall, J. W., Batista, I. S., Sobral, J. H. A., and Jayachandran, P. T. (2003). Equatorial evening prereversal electric field enhancement and sporadic *E* layer disruption: A manifestation of *E* and *F* region coupling. *J. Geophys. Res.: Space Phys.*, *108*(A6), 1254. https://doi.org/10.1029/2002JA009285

Abdu, M. A., Nogueira, P. A. B., Santos, A. M., de Souza, J. R., Batista, I. S., and Sobral, J. H. A. (2018). Impact of disturbance electric fields in the evening on prereversal vertical drift and spread F developments in the equatorial ionosphere. *Ann. Geophys.*, *36*(2), 609–620. https://doi.org/10.5194/angeo-36-609-2018

Benjamini, Y., and Hochberg, Y. (1995). Controlling the false discovery rate: A practical and powerful approach to multiple testing. *J. Roy. Stat. Soc.: Ser. B (Methodol.)*, *57*(1), 289–300. https://doi.org/10.1111/j.2517-6161.1995.tb02031.x

Gao, P. D., Zhu, Q. Y., Cai, J. H., Wang, Z., Wang, G. J., Zhan, M. Y., Qi, Q., Shi, J. K., Qiu, C., … Ding, K. (2026). A deep learning-enabled ionogram dataset for detection and classification of low-latitude spread-F phenomena. *Sci. Data*, *13*(1), 181. https://doi.org/10.1038/s41597-025-06493-5

Haldoupis, C. (2011). A tutorial review on sporadic *E* layers. In M. A. Abdu et al. (Eds.), *Aeronomy of the Earth's Atmosphere and Ionosphere* (pp. 381–394). Dordrecht, Netherlands: Springer. https://doi.org/10.1007/978-94-007-0326-1_29

Haldoupis, C. (2019). An improved ionosonde-based parameter to assess sporadic E layer intensities: A simple idea and an algorithm. *J. Geophys. Res.: Space Phys.*, *124*(3), 2127–2134. https://doi.org/10.1029/2018JA026441

Huber, P. J. (1964). Robust estimation of a location parameter. *Ann. Math. Stat.*, *35*(1), 73–101. https://doi.org/10.1214/aoms/1177703732

Hysell, D. L., Larsen, M. F., Swenson, C. M., Barjatya, A., Wheeler, T. F., Sarango, M. F., Woodman, R. F., and Chau, J. L. (2005). Onset conditions for equatorial spread *F* determined during EQUIS II. *Geophys. Res. Lett.*, *32*(24), L24104. https://doi.org/10.1029/2005GL024743

Kelley, M. C., Haldoupis, C., Nicolls, M. J., Makela, J. J., Belehaki, A., Shalimov, S., and Wong, V. K. (2003). Case studies of coupling between the *E* and *F* regions during unstable sporadic-*E* conditions. *J. Geophys. Res.: Space Phys.*,

108(A12), 1447. https://doi.org/10.1029/2003JA009955

Lee, C. C., and Chen, W. S. (2018). Effects of sporadic E-layer characteristics on spread-F generation in the nighttime midlatitude ionosphere: A climatological study. *J. Atmos. Solar-Terr. Phys.*, *169*, 130–137. https://doi.org/10.1016/j.jastp.2018.02.002

Reinisch, B. W., Abdu, M., Batista, I., Sales, G. S., Khmyrov, G., Bullett, T. A., Chau, J., and Rios, V. (2004). Multistation digisonde observations of equatorial spread F in South America. *Ann. Geophys.*, *22*(9), 3145–3153. https://doi.org/10.5194/angeo-22-3145-2004

Shalimov, S., and Haldoupis, C. (2005). *E*-region wind-driven electrical coupling of patchy sporadic-*E* and spread-*F* at midlatitude. *Ann. Geophys.*, *23*(6), 2095–2105. https://doi.org/10.5194/angeo-23-2095-2005

Shi, J. K., Wang, G. J., Reinisch, B. W., Shang, S. P., Wang, X., Zherebotsov, G., and Potekhin, A. (2011). Relationship between strong range spread *F* and ionospheric scintillations observed in Hainan from 2003 to 2007. *J. Geophys. Res.: Space Phys.*, *116*(A8), A08306. https://doi.org/10.1029/2011JA016806

Stephan, A. W., Colerico, M., Mendillo, M., Reinisch, B. W., and Anderson, D. (2002). Suppression of equatorial spread *F* by sporadic *E*. *J. Geophys. Res.: Space Phys.*, *107*(A2), SIA 4-1–SIA 4-5. https://doi.org/10.1029/2001JA000162

Tsunoda, R. T. (2007). Seeding of equatorial plasma bubbles with electric fields from an E_s-layer instability. *J. Geophys. Res.: Space Phys.*, *112*(A6), A06304. https://doi.org/10.1029/2006JA012103

Wang, G. J., Shi, J. K., Wang, X., Shang, S. P., Zherebtsov, G., and Pirog, O. M. (2010). The statistical properties of spread F observed at Hainan station during the declining period of the 23rd solar cycle. *Ann. Geophys.*, *28*(6), 1263–1271. https://doi.org/10.5194/angeo-28-1263-2010

Wang, G. J., Shi, J. K., Reinisch, B. W., Wang, X., and Wang, Z. (2015). Ionospheric plasma bubbles observed concurrently by multi-instruments over low-latitude station Hainan. *J. Geophys. Res.: Space Phys.*, *120*(3), 2288–2298. https://doi.org/10.1002/2014JA020245

Wang, Z., Zhan, M. Y., Gao, P. D., Wang, G. J., Qiu, C., Qi, Q., Shi, J. K., and Wang, X. (2023). Automatic detection and classification of spread-F from ionosonde at Hainan with image-based deep learning method. *Space Wea.*, *21*(11), e2023SW003498. https://doi.org/10.1029/2023SW003498

Wang, Z., and Wang, G. J. (2026). Aggregate results for sporadic E conditions associated with four spread F morphologies over Hainan (Version 1) [Dataset]. Science Data Bank. https://doi.org/10.57760/sciencedb.012m9

Zhang, Y., Wan, W., Li, G., Liu, L., Hu, L., and Ning, B. (2015). A comparative study of GPS ionospheric scintillations and ionogram spread F over Sanya. *Ann. Geophys.*, *33*(11), 1421–1430. https://doi.org/10.5194/angeo-33-1421-2015